

Reconstructing QCD Spectral Functions with Gaussian Processes

Jan Horak,¹ Jan M. Pawłowski,^{1,2} José Rodríguez-Quintero,³ Jonas Turnwald,¹
Julian M. Urban,^{1,*} Nicolas Wink,¹ and Savvas Zafeiropoulos⁴

¹*Institut für Theoretische Physik, Universität Heidelberg, Philosophenweg 16, D-69120 Heidelberg, Germany*

²*ExtreMe Matter Institute EMMI, GSI, Planckstr. 1, D-64291 Darmstadt, Germany*

³*Department of Integrated Sciences and Center for Advanced Studies in Physics, Mathematics and Computation, University of Huelva, E-21071 Huelva, Spain*

⁴*Aix Marseille Univ, Université de Toulon, CNRS, CPT, Marseille, France*

We reconstruct ghost and gluon spectral functions in 2+1 flavor QCD with Gaussian process regression. This framework allows us to largely suppress spurious oscillations and other common reconstruction artifacts by specifying generic magnitude and length scale parameters in the kernel function. The Euclidean propagator data are taken from lattice simulations with domain wall fermions at the physical point. For the infrared and ultraviolet extensions of the lattice propagators as well as the low-frequency asymptotics of the ghost spectral function, we utilize results from functional computations in Yang-Mills theory and QCD. This further reduces the systematic error significantly. Our numerical results are compared against a direct real-time functional computation of the ghost and an earlier reconstruction of the gluon in Yang-Mills theory. The systematic approach presented in this work offers a promising route towards unveiling real-time properties of QCD.

Introduction. The resolution of many open questions in quantum chromodynamics (QCD) requires the knowledge of time-like observables and hence the computation of real-time correlation functions. Applications range from the hadronic resonance spectrum over scattering processes to transport and non-equilibrium phenomena in heavy-ion collisions. For example, the computation of the glueball spectrum via Bethe-Salpeter equations relies on the time-like propagators for gluon and ghost, both of which are reconstructed in the present work. Likewise, QCD transport coefficients used in hydrodynamic simulations can be computed diagrammatically from the real-time gluon propagator. Similarly, phenomenological QCD transport models with their underlying assumption of a quasi-particle nature of the gluon can hugely benefit in multiple ways from the present results. First of all, a reliable computation of the gluon spectral function may offer much-needed support for the quasi-particle assumption of these models, as well as give access to its limitations. Secondly, the QCD gluon spectral function itself can feature as a direct input and pivotal building block in these models. Together with further time-like correlation functions, this offers a path for a systematic quantitative improvement of phenomenological transport approaches towards first-principle transport in QCD.

By now, Euclidean correlation functions in QCD are accessible within first-principle approaches such as lattice simulations or functional equations. In contradistinction, accessing real-time properties remains a notoriously hard task. Minkowski correlation functions may be obtained from Euclidean data via spectral reconstruction, exploiting the Källén-Lehmann (KL) representation [1, 2]. This requires computing the spectral function via an inverse integral transform. In the present work, we approach the

problem with Gaussian process regression (GPR). The applicability of GPR to inverse problems of this type has been discussed in [3]. Specifically, it was shown how GPs can be used to obtain probabilistic models of functions for which only weighted averages are available.

We apply GPR to the reconstruction of ghost and gluon spectral functions based on recent results from 2+1 flavor lattice QCD with domain wall fermions at a pion mass of 139 MeV [4, 5]. Furthermore, we improve the systematic error control by incorporating additional results from functional renormalization group (fRG) and Dyson-Schwinger (DSE) computations in Yang-Mills theory and QCD [6–12], mostly obtained within the fQCD collaboration [13].

Spectral representation. The KL spectral representation of the two-point correlation function in momentum space reads

$$G(p_0) = \int_0^\infty \frac{d\omega}{\pi} \frac{\omega \rho(\omega)}{\omega^2 + p_0^2} = \int_0^\infty d\omega K(p_0, \omega) \rho(\omega), \quad (1)$$

with the KL kernel $K(p_0, \omega)$ and $\rho(-\omega) = -\rho(\omega)$. In the vacuum, the spatial momentum dependence of the propagator can be obtained via a Lorentz boost, simply by $p_0^2 \rightarrow p^2$ with $p^2 = p_0^2 + \vec{p}^2$.

With Equation (1), the spectral function is obtained from the retarded propagator via

$$\rho(\omega) = 2 \operatorname{Im} G(-i(\omega + i0^+)). \quad (2)$$

For asymptotic states, the spectral function is the probability density for (multi-)particle excitations created from the vacuum in the presence of the corresponding quantum field. Consequently, in this case the spectral function is positive semi-definite. For propagators of ‘unphysical’ fields, such as gauge fields, the spectral representation may still hold. However, the spectral function can then also have negative parts, and the existence of a spec-

* urban@thphys.uni-heidelberg.de; corresponding author.

tral representation simply constrains the allowed complex structure of correlation functions; see e.g. [8, 12, 14–16].

In this work, we reconstruct ghost and gluon spectral functions of 2+1 flavor QCD under the assumption that both admit a KL representation. It can be shown that the total spectral weight vanishes,

$$\int_0^\infty \frac{d\omega}{\pi} \omega \rho_{A/c}(\omega) = 0, \quad (3)$$

respectively for both the ghost and gluon spectral functions, ρ_c and ρ_A . For the gluon, this is the well-known Oehme-Zimmermann superconvergence (OZS) condition [17, 18]; for recent discussions with general fields, see [8, 12, 16]. These works also include a treatment of the analytic low-frequency behavior of continuous parts of the spectral functions, initiated in [8].

A general spectral function ρ consists of a continuous part $\tilde{\rho}$ and a sum of particle and resonance peaks (proportional to the δ -function and its derivatives). The gluon spectral function only consists of a continuous part $\rho_A = \tilde{\rho}_A$ satisfying Equation (3). In turn, the ghost spectral function also exhibits a particle peak at vanishing frequency due to the infrared $1/p^2$ behavior of the Euclidean lattice ghost propagator,

$$\rho_c(\omega) = \frac{\pi}{Z_c} \frac{\delta(\omega)}{\omega} + \tilde{\rho}_c(\omega), \quad \int_0^\infty \frac{d\omega}{\pi} \omega \tilde{\rho}_c(\omega) = -\frac{1}{Z_c}, \quad (4)$$

where $\delta(\omega)/\omega$ has to be understood as a limiting process $\delta(\omega - m)/\omega$ with $m \rightarrow 0^+$. Evidently, for $Z_c = 1$ and $\tilde{\rho}_c = 0$ the ghost propagator reduces to the classical one. This concludes our brief discussion of the formal properties of ghost and gluon spectral functions.

Euclidean correlators obtained from lattice simulations are generally only available in terms of discrete sets of observations G_i at N_G Euclidean momenta p_i with finite precision. Relating the results to the associated Minkowski propagators via Equation (2) is problematic; see e.g. [19, 20]. In such a numerical setup the analytic continuation via $p \rightarrow -i(\omega + i0^+)$ is ill-conditioned, since further assumptions about the complex structure need to be made. Instead, the usual strategy is the numerical inversion of the integral transformation. A variety of approaches has been explored to tackle this issue, such as the maximum entropy method [21–23], Bayesian inference techniques [24, 25], suitable expansions in functional spaces [8, 19, 20, 26, 27], Padé-type approximants [28], Tikhonov regularization [29–31], neural networks [32–35], and kernel ridge regression [36, 37].

Reconstruction with GPR. Starting from early developments in the context of geostatistics in the 1950s [38], today GPR is widely employed in a variety of settings for the probabilistic modeling of functions from a finite number of observations; see [39, 40] for recent reviews and [41] for a modern textbook account. Here we summarize the main ingredients for spectral reconstruction with GPR based on the developments reported in [3]. A short introduction to GPR for function prediction as

well as further details and references are provided in Appendix A.

We assume our knowledge of the spectral function $\rho(\omega)$ to be described by a GP, written as

$$\rho(\omega) \sim \mathcal{GP}(\mu(\omega), C(\omega, \omega')), \quad (5)$$

where $\mu(\omega), C(\omega, \omega')$ denote the mean and covariance functions. Importantly, in this approach we do not restrict the space of possible solutions by choosing a specific functional basis, which often leads to spurious artifacts in the reconstruction in order to compensate for unrepresentable features. Instead, the GP defines a distribution over families of functions with rather generic properties, specified via the kernel parametrization described below.

The KL integral in Equation (1) is a linear transformation that preserves Gaussian statistics. Hence, with Equation (5) one may obtain statistical predictions G_i at N_G specified momenta p_i as

$$\begin{aligned} G_i &\sim \mathcal{N} \left(\int d\omega K(p_i, \omega) \mu(\omega), \right. \\ &\quad \left. \int d\omega d\omega' K(p_i, \omega) C(\omega, \omega') K(p_j, \omega') \right) \\ &\equiv \mathcal{N}(\tilde{\mu}_i, \tilde{C}_{ij}). \end{aligned} \quad (6)$$

Here, \mathcal{N} denotes a multivariate normal distribution, to be distinguished from distributions over function space denoted by \mathcal{GP} . Statistical uncertainties associated with individual prediction points $\tilde{\mu}_i$ may be computed from the diagonal of the covariance matrix as $\tilde{\sigma}_i = \sqrt{\tilde{C}_{ii}}$.

Conversely, the framework also enables inference in the opposite direction. The inherent analytic tractability associated with Gaussian statistics allows formulating the conditional distribution for $\rho(\omega)$ given observations G_i in closed form. The full expression may then be derived as

$$\begin{aligned} \rho(\omega) | G_i &\sim \mathcal{GP} \left(\mu(\omega) + \right. \\ &\quad \left. \sum_{i,j=1}^{N_G} \int d\omega' K(p_i, \omega') C(\omega', \omega) \left(\tilde{C} + \sigma_n^2 \cdot \mathbf{1} \right)_{ij}^{-1} (G_j - \tilde{\mu}_j), \right. \\ &\quad \left. C(\omega, \omega') - \sum_{i,j=1}^{N_G} \int d\omega' d\omega'' K(p_i, \omega') C(\omega', \omega) \right. \\ &\quad \left. \left(\tilde{C} + \sigma_n^2 \cdot \mathbf{1} \right)_{ij}^{-1} K(p_j, \omega'') C(\omega'', \omega) \right). \end{aligned} \quad (7)$$

The GP in Equation (7) encodes our knowledge of the spectral function after making observations of the propagator and accounting for observational noise with variance σ_n^2 . The corresponding expressions for the dressing function instead of the propagator can be immediately obtained by inserting an additional factor of p_i^2 at every occurrence of the KL kernel $K(p_i, \omega)$.

The flexibility of the approach makes it possible to also incorporate further available prior information in various

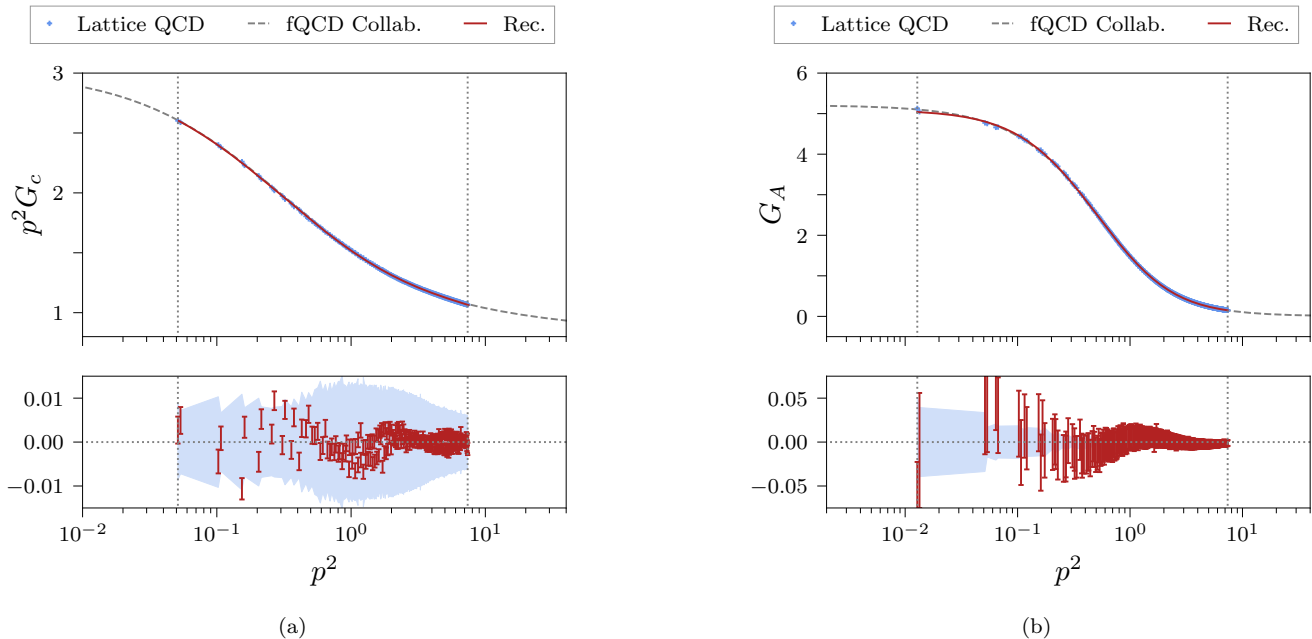


FIG. 1. Plots showing the ghost dressing function (a) and gluon propagator (b) from 2+1 flavor lattice QCD simulations, extended by functional computations in Yang-Mills theory and QCD and compared against the correlators obtained from the reconstructed spectral functions shown in Figure 2. The results agree within the given statistical uncertainties as shown in the bottom panels, where the posterior GPs for the correlators are evaluated at the fixed momenta provided by the lattice data, which is then subtracted leaving the error bars intact. The total mean squared errors amount to $\sim 5e-6$ for the ghost and $\sim 4e-5$ for the gluon.

forms into the predictive distribution in the same manner, yielding similar though somewhat more complicated expressions. This may include e.g. direct observations of ρ and its derivatives, assumptions about the asymptotic behavior, or global normalization constraints.

In order for GPs to be useful for modeling, the covariance $C(\omega, \omega')$ may be defined via a so-called kernel function. It is commonly parametrized using a small number of hyperparameters, which may be subjected to optimization based on the associated likelihood. The mean function $\mu(\omega)$ is often set to zero as its contribution can be fully absorbed by the kernel. Typically, the latter is the sole focus of the optimization procedure. However, a custom mean function may still be useful in certain situations in order to incorporate prior beliefs about the expected solution.

A commonly used kernel parametrization is the radial basis function (RBF) kernel, also called squared exponential. It is defined as

$$C(\omega, \omega') = \sigma_C^2 \exp\left(-\frac{(\omega - \omega')^2}{2l^2}\right), \quad (8)$$

where the parameter σ_C controls the overall magnitude and l is a generic length scale. The RBF kernel has been established as the standard choice for many applications due to a number of attractive features. It is also used for our first results on spectral reconstruction with GPR presented in this work.

Nevertheless, designing custom kernels for specific problems has been shown to greatly increase the usefulness of the approach in various settings and is also promising here. In particular, it may be interesting to construct kernel functions that can be integrated analytically against the KL kernel, such that the frequency integrals in Equations (6) and (7) may be carried out analytically instead of numerically. To this end, one could potentially employ functions of Breit-Wigner type as done for the spectral function itself in [8]. In contradistinction, we may use them to instead define a suitable GP kernel, thereby still avoiding the restriction to a specific functional basis as previously mentioned. We comment on this and other possible improvements to our reconstruction approach in the conclusion.

Furthermore, we emphasize that the present approach in principle does not require us to choose a specific set of nodes ω_i . In fact, instead of computing a discrete set of point predictions or coefficients of a predefined functional basis, the prediction for ρ is obtained as a function of ω , albeit only implicitly via the kernel formulation. In particular, the GP also enables access to all of the derivatives of the prediction at any point. A finite set of nodes ω_i is chosen only at inference time in order to evaluate the GP, however, the choice is completely arbitrary within the given domain. This property is one of the most attractive features of GPR for spectral reconstruction and probabilistic function prediction in general.

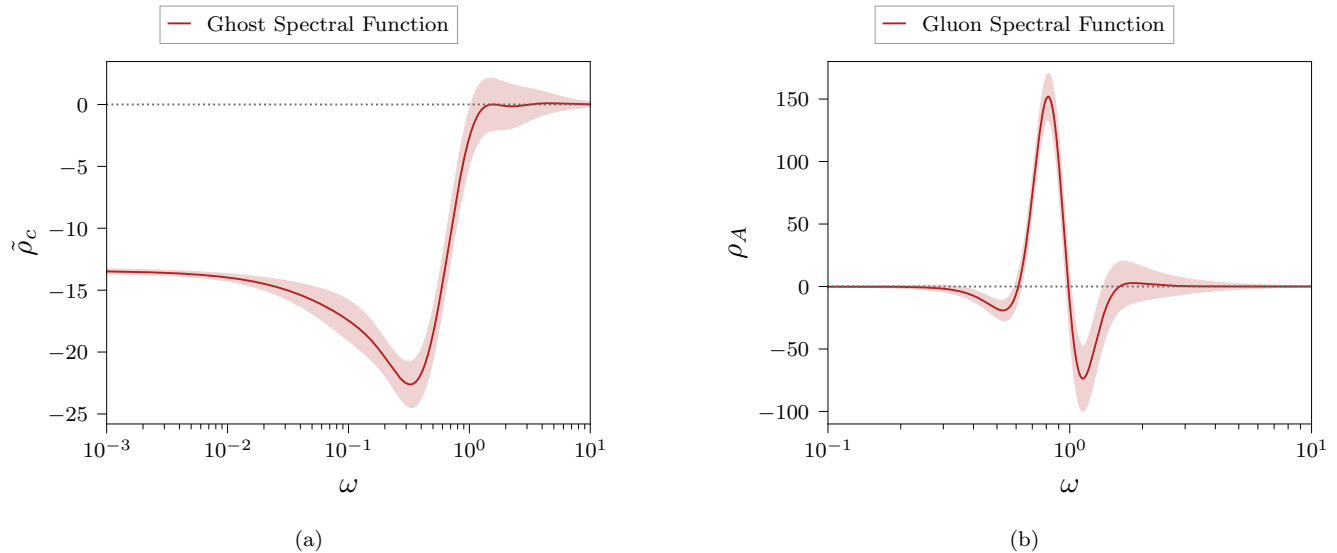


FIG. 2. Plots showing the continuous part of the ghost (a) and the gluon spectral function (b) reconstructed from the lattice QCD correlators shown in Figure 1 using GPR. Shaded areas represent the 1σ -bands of plausible solutions around the mean prediction based on the available observations and precision. The ghost spectral function ρ_c features an additional massless particle pole in the origin; cf. Equation (4).

Input Data. In the past two decades, increasing interest in the momentum behavior of the fundamental two-point Green’s functions in QCD as well as further correlation functions of higher order has triggered respective lattice calculations in particular of Yang-Mills and QCD propagators; see e.g. [42–56]. The lattice data for the ghost dressing function and gluon propagator employed in this work, shown in Figure 1, are obtained from recent simulations of 2+1 flavor QCD at the physical point [4, 5]; see Appendix B 1 for further details and references. Additional input data and benchmarks are provided by results from functional computations in Yang-Mills theory and QCD [6, 8, 11, 12], shown in Figures 3 and 4; see Appendix B 2 for details. Extending the lattice data using functional methods improves the stability and systematic error of the reconstruction.

Reconstruction Results. The GPR for the reconstruction of the ghost spectral function is performed using the aforementioned standard RBF kernel. We fix the low-frequency asymptotics of the spectral function with the direct real-time DSE result in Yang-Mills theory [12] by treating it as an additional observation. The kernel’s hyperparameters are chosen by optimizing the associated likelihood of observations with an additional Gaussian hyperprior, which we achieve through a fine-grained grid scan; see Appendix C for details. The reconstructed spectral function in Figure 2a accurately reproduces the dressing function data within the uncertainties displayed in Figure 1a, with a total mean squared error of $\sim 5e-6$.

The features of our prediction are strikingly similar to the aforementioned Yang-Mills result shown in Figure 4a in Appendix B, even though only the infrared limit is

incorporated into the reconstruction. This similarity is expected heuristically, since the ghost only interacts with the quarks indirectly via the gluon vertices, and the effects of introducing dynamical quarks must hence be of higher order. This qualitative similarity is particularly notable considering that the methods are conceptually very different.

For the reconstruction of the gluon spectral function, a modified frequency scale is used in the RBF kernel in order to suppress spurious oscillations in the infrared and ultraviolet tails. The hyperparameters are again obtained via optimization of the likelihood with Gaussian hyperpriors while approximately enforcing the OZS condition; see Appendix C for details. The reconstruction shown in Figure 2b accurately reproduces the lattice data within the given uncertainties, as shown in Figure 1b, with a total mean squared error of $\sim 4e-5$. While also being fully consistent, deviations from the lattice propagator are somewhat stronger than for the ghost dressing function and seem to become more pronounced in the infrared. This is likely caused by the comparably large uncertainties of the lattice data at small momenta.

The peak structure of the spectral function appears similar to an earlier reconstruction from the Yang-Mills propagator in the fRG framework [8], shown in Figure 4b in Appendix B. We also emphasize that the reconstruction is based on a UV extension with the Yang-Mills data of [6] instead of the full 2+1 flavor results from [11]. This is detailed in Appendix B 2 and facilitates the comparison with the Yang-Mills reconstruction [8]. In particular, the positions of the leading positive peaks approximately coincide, with $\omega \approx 0.818$ for the present result and $\omega \approx 0.835$ for the fRG reconstruction. This re-

flects the approximate coincidence of the peaks of the Euclidean gluon dressing functions shown in [Figure 3a](#) in [Appendix B](#). We also note that a small peak to the right of the second local minimum is present in both reconstructions. This feature may be a generic reconstruction artifact since it is not necessitated by theoretical considerations, but is observed in both results from conceptually very distinct methods. However, the comparably large uncertainties in this region also include plausible solutions without additional zero-crossings.

Significant differences between the two reconstructions are observed mainly in the overall peak height and width. Generally, the QCD result for the gluon is expected to differ more strongly from the pure gauge theory than the ghost due to the direct coupling to quarks. However, differences may also be attributed in part to the limited availability and precision of data and the resulting difficulty in resolving highly peaked structures. We find that generating narrower peaks with greater amplitudes by allowing the kernel's magnitude parameter σ_C to increase and the length scale l to decrease leads to stronger oscillations in the solution, a common feature of many reconstruction approaches. Regulating these hyperparameters to deliberately suppress such unphysical features may result in reconstructions that are naturally flatter, which must be taken into account when interpreting and utilizing the result. This demonstrates one of the key advantages of GPR, namely the possibility to dynamically adjust the resolution depending on the available amount and quality of the input data, while still reproducing the observations as accurately as possible.

Conclusion. In this work, we have applied Gaussian process regression to the reconstruction of ghost and gluon spectral functions in 2+1 flavor QCD at the physical point. These spectral functions are the pivotal building blocks of diagrammatic representations for bound state equations such as Bethe-Salpeter and Faddeev equations, see e.g. [\[57–59\]](#), as well as transport coefficients, see e.g. [\[23, 60\]](#).

Importantly, the gluon spectral function has a pronounced quasi-particle peak, the position of which is related to the mass gap in QCD. This extends previous vacuum and finite-temperature results in Yang-Mills theory [\[8, 23\]](#) to physical QCD. Our findings provide non-trivial QCD support to the phenomenological use of quasi-particle gluon spectral functions for transport computations; for a recent review, see [\[61\]](#). Moreover, the present results can be directly employed as first-principle QCD inputs in order to systematically improve the respective phenomenological approaches towards a first-principle treatment of QCD transport processes.

These promising phenomenological applications of the present results also highlight the necessity of further improving the reconstruction approach itself, for which a number of potential directions can be envisaged. This includes the aforementioned possibility of designing cus-

tom kernels for the problem at hand, potentially with analytic integrability against the KL kernel. Constructing suitable, expressive kernels may also be automated and improved through the use of hyperkernels [\[62\]](#) or techniques such as deep kernel learning [\[63\]](#). To account for some variability in the kernel hyperparameters, one may replace the maximum likelihood approach by an integral over parameter space using a suitable hyperprior which encodes any prior assumptions. Alternatively, optimal hyperparameters may also be selected based on a data-driven machine learning approach, using datasets consisting of pairs of correlators and associated spectral functions.

Furthermore, the flexibility of the GPR framework allows the incorporation of various supplementary constraints derived from theoretical arguments, such as information about derivatives, known asymptotic behaviors, or normalization conditions. This is expected to further improve the accuracy and reliability of the reconstruction and will be the subject of future research, accompanied by direct functional computations of further spectral properties along the lines of [\[12, 64\]](#).

The immediate next steps in our endeavor towards unveiling real-time properties of QCD are the application and extension of the present numerical method to quark propagators as well as correlation functions computed at finite temperature. This will enable quantitative studies of hitherto theoretically inaccessible non-equilibrium dynamics of QCD in the transport phase of heavy-ion collisions within a first-principle approach.

Acknowledgements. We thank A. Cyrol, F. Gao, L. Kades, J.Y. Lin, J. Papavassiliou and A. Rothkopf for discussions. We thank P. Boucaud and F. De Soto for an earlier collaboration and for their help in the preparation of the lattice data. We are indebted to the RBC/UKQCD collaboration, especially to P. Boyle, N. Christ, Z. Dong, N. Garron, C. Jung, B. Mawhinney and O. Witzel, for access to the lattices used in this work. We also thank the members of the fQCD collaborations for discussions and collaborations on related subjects. JRQ acknowledges the support of MICINN PID2019-107844GB-C22 grant. Numerical computations have used resources of CINES, GENCI IDRIS (project id 52271) and of the IN2P3 computing facility in France. This work is supported by the Deutsche Forschungsgemeinschaft (DFG, German Research Foundation) under Germany's Excellence Strategy EXC 2181/1 - 390900948 (the Heidelberg STRUCTURES Excellence Cluster), under the Collaborative Research Centre SFB 1225 (ISOQUANT), EMMI, and the BMBF grant 05P18VHFCA.

Appendix A: Introduction to GPR

This appendix serves as a brief introduction to GPR for function prediction using a finite number of direct or indirect observations, based primarily on [3]. We adopt the notation used in the main text for consistency, however, the general formalism presented here is also applicable outside of the specific context of spectral reconstruction for quantum field theory. For a modern, comprehensive textbook treatment of the topic, we refer the interested reader to [41]. For a brief, pedagogical introduction to GPR with simple code examples, we recommend [65]. In the context of inverse theory, [66] provides a recent review.

We first discuss GPR for the case where direct observations are available for the function to be modeled. We assume our knowledge of the function $\rho(\omega)$ to be encoded in a GP with mean and covariance functions $\mu(\omega)$, $C(\omega, \omega')$, denoted by

$$\rho(\omega) \sim \mathcal{GP}(\mu(\omega), C(\omega, \omega')) , \quad (\text{A1})$$

where the covariance is assumed to be symmetric, i.e. $C(\omega, \omega') = C(\omega', \omega)$. As per the definition of a GP, any finite set of function evaluations at N sample points ω_i follows a multivariate normal distribution,

$$\begin{pmatrix} \rho(\omega_1) \\ \vdots \\ \rho(\omega_N) \end{pmatrix} \sim \mathcal{N} \left(\begin{pmatrix} \mu(\omega_1) \\ \vdots \\ \mu(\omega_N) \end{pmatrix}, \begin{pmatrix} C(\omega_1, \omega_1) & \dots & C(\omega_1, \omega_N) \\ \vdots & \ddots & \vdots \\ C(\omega_N, \omega_1) & \dots & C(\omega_N, \omega_N) \end{pmatrix} \right) . \quad (\text{A2})$$

Similarly, we can write down the joint distribution of a set of observations $\hat{\rho}_i$ at points $\hat{\omega}_i$ and the value of the function at an arbitrary point ω as

$$\begin{pmatrix} \rho(\omega) \\ \hat{\rho} \end{pmatrix} \sim \mathcal{N} \left(\begin{pmatrix} \mu(\omega) \\ \hat{\mu} \end{pmatrix}, \begin{pmatrix} C(\omega, \omega) & \hat{\mathbf{C}}^T(\omega) \\ \hat{\mathbf{C}}(\omega) & \hat{\mathbf{C}} + \sigma_n^2 \cdot \mathbf{1} \end{pmatrix} \right) , \quad (\text{A3})$$

where boldface type denotes vector and matrix quantities. Here, we have defined $\hat{\mu} \equiv \mu(\hat{\omega}_i)$, $\hat{\mathbf{C}}_i(\omega) \equiv C(\hat{\omega}_i, \omega)$, and $\hat{\mathbf{C}}_{ij} \equiv C(\hat{\omega}_i, \hat{\omega}_j)$. σ_n^2 defines the point-wise variance of additional measurement noise which may be present in the observations $\hat{\rho}$. Due to the analytic tractability of multivariate Gaussians, the conditional distribution of function values $\rho(\omega)$ given observations $\hat{\rho}$ may then be derived as

$$\begin{aligned} \rho(\omega) | \hat{\rho} \sim \mathcal{N} \left(\mu(\omega) + \hat{\mathbf{C}}^T(\omega) \left(\hat{\mathbf{C}} + \sigma_n^2 \cdot \mathbf{1} \right)^{-1} (\hat{\rho} - \hat{\mu}) , \right. \\ \left. C(\omega, \omega) - \hat{\mathbf{C}}^T(\omega) \left(\hat{\mathbf{C}} + \sigma_n^2 \cdot \mathbf{1} \right)^{-1} \hat{\mathbf{C}}(\omega) \right) . \end{aligned} \quad (\text{A4})$$

The covariance is parametrized by a suitable kernel function, whereby one may encode any prior beliefs about the types of solutions one expects by choosing an appropriate form for the problem at hand. For an introduction to constructing GP kernels of various types as well as strategies to apply and combine them, we recommend the kernel cookbook [67].

A kernel's hyperparameters, denoted here by $\hat{\alpha}$, may be subjected to optimization by maximizing the associated likelihood,

$$\begin{aligned} p(\hat{\rho} | \alpha) = \left((2\pi)^N \det \left(\hat{\mathbf{C}}_\alpha + \sigma_n^2 \cdot \mathbf{1} \right) \right)^{-\frac{1}{2}} \\ \exp \left(-\frac{1}{2} (\hat{\rho} - \hat{\mu})^T \left(\hat{\mathbf{C}}_\alpha + \sigma_n^2 \cdot \mathbf{1} \right)^{-1} (\hat{\rho} - \hat{\mu}) \right) , \end{aligned} \quad (\text{A5})$$

where we have written $\hat{\mathbf{C}}_\alpha$ to emphasize the dependence on the hyperparameters. Instead of directly maximizing $p(\hat{\rho} | \alpha)$ as a function of $\hat{\alpha}$, one conventionally minimizes the negative log likelihood (NLL),

$$\begin{aligned} -\log p(\hat{\rho} | \alpha) = \frac{1}{2} (\hat{\rho} - \hat{\mu})^T \left(\hat{\mathbf{C}}_\alpha + \sigma_n^2 \cdot \mathbf{1} \right)^{-1} (\hat{\rho} - \hat{\mu}) \\ + \frac{1}{2} \log \det \left(\hat{\mathbf{C}}_\alpha + \sigma_n^2 \cdot \mathbf{1} \right) + \frac{N}{2} \log 2\pi . \end{aligned} \quad (\text{A6})$$

Since simply finding and employing the maximum likelihood configuration of hyperparameters may ignore relevant additional structures in the distribution, one can also integrate out $\hat{\alpha}$ using suitable hyperpriors to account for some variability.

Based on the formulation of GPR for direct observations $\hat{\rho}$ at points $\hat{\omega}$, one can derive the expressions for inference from indirect observations $\hat{\mathbf{G}}$ at points $\hat{\mathbf{p}}$ as discussed in the main text by applying the forward process of the associated linear inverse problem, in our case the KL integral defined in Equation (1). This involves all terms related to the observations that depend on the discrete set of points $\hat{\omega}$, which are promoted back to the continuous domain and subsequently integrated out to yield the nodes $\hat{\mathbf{p}}$ instead.

Appendix B: Input Data

Combining the data from lattice simulations and functional computations as described in the main text requires matching the scales through renormalization. In this work, we always rescale the functional methods results to match the lattice data in the appropriate regime.

1. Lattice Simulations

The lattice data employed in this work for the reconstruction were obtained from lattice configurations generated by the RBC/UKQCD collaboration, and firstly introduced in [68–72], with 2+1 dynamical quark flavors

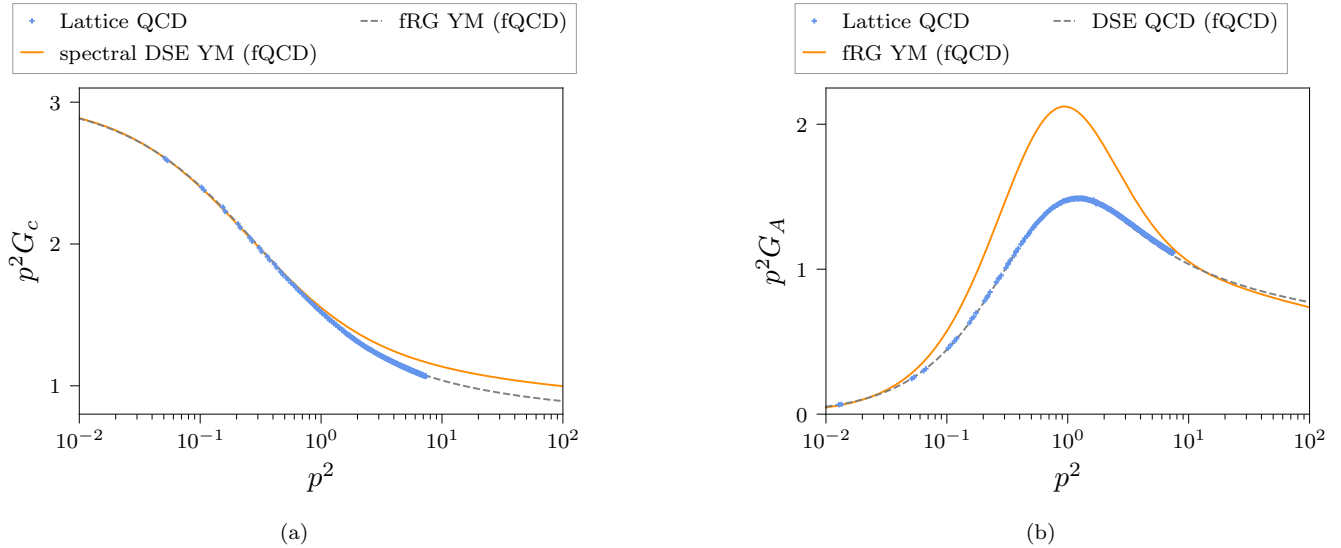


FIG. 3. Plots showing ghost (a) and gluon (b) dressing functions in 2+1 flavor QCD and Yang-Mills (YM) theory, obtained from the lattice simulations and functional computations discussed in [Appendix B](#).

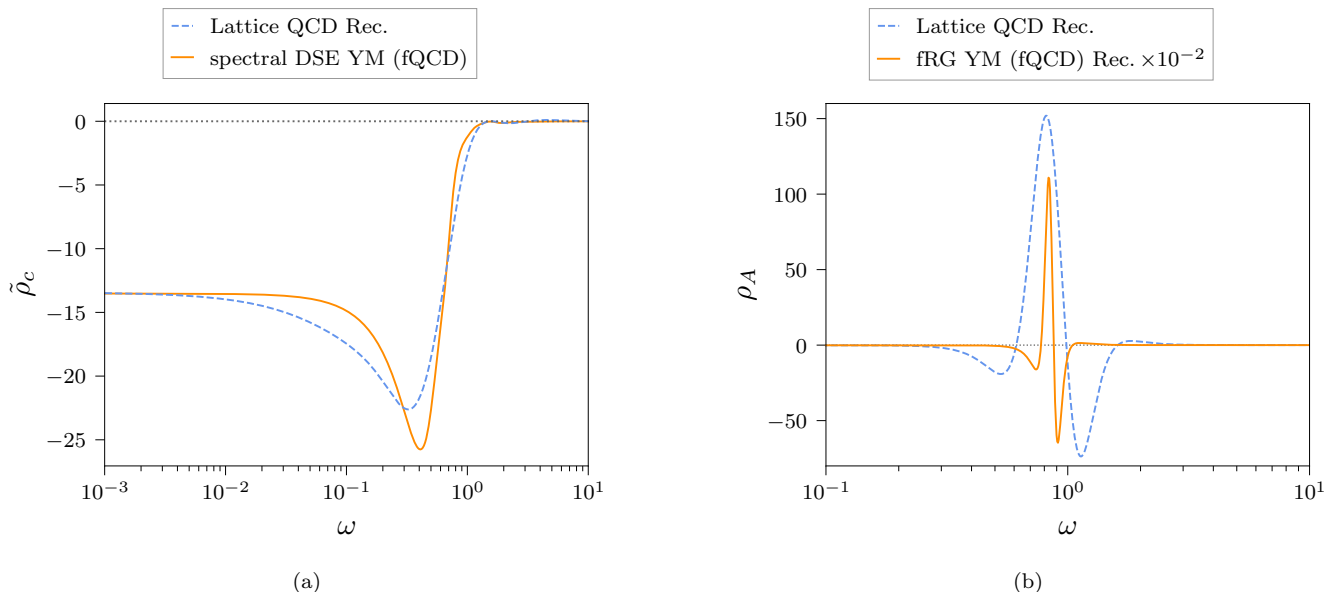


FIG. 4. Plots comparing the continuous part of the ghost (a) and the gluon spectral function (b) from different approaches in 2+1 flavor QCD and Yang-Mills (YM) theory, as discussed in the results section and [Appendix B](#). The ghost spectral function ρ_c features an additional massless particle pole in the origin; cf. [Equation \(4\)](#).

using the Iwasaki [73] and domain wall fermion [74, 75] actions, respectively for the gauge and quark sectors, at the physical point (a pion mass amounting to 139 MeV) by the particular implementation of the Möbius kernel [76]. These developments were then exploited in [4, 5] in order to calculate the gluon and ghost propagators as well as the strong coupling in a particular scheme [77–79], and an effective charge stemming from it [80]. A description of this calculation is given, for instance, in [51].

In computing propagators that properly feature the physical running with momenta, data should be thoroughly cured from lattice regularization artifacts. In particular, as explained in [4], our results are obtained after a careful scrutiny of discretization artifacts, thereby accounting for the continuum-limit extrapolation, following [81]. As a noteworthy remark, a recent work [56] has revealed the key role played by the procedure of [81] for an adequate removal of discretization artifacts in achiev-

ing a consistent description of Yang-Mills two- and three-point correlators, involving both lattice and DSE results.

The resulting ghost dressing function and gluon propagator data are displayed in [Figures 1a](#) and [1b](#), respectively. They are compared against their counterparts obtained from evaluating [Equation \(1\)](#) for the reconstructed spectral functions shown in [Figure 2](#), as well as the results from functional methods described in the following section. The dressing functions of all input datasets are compared in [Figure 3](#) to further illustrate their similarities and differences.

2. Functional Methods

We briefly summarize results from functional computations in Yang-Mills theory and QCD that are employed in this work to provide additional prior information for the reconstruction. For reviews on the application of functional methods in this context, see e.g. [\[82–85\]](#).

We use the real-time Yang-Mills results from [\[12\]](#) to extend the lattice QCD data of the ghost dressing function into the deep infrared, as shown in [Figure 3a](#). The approach also provides direct access to the associated spectral function, which we employ to fix the low-frequency asymptotic behavior of the reconstruction. It is obtained via the spectral ghost DSE, building upon the technique of spectral renormalization [\[64\]](#). Making use of [Equation \(1\)](#) for the ghost and gluon propagator, the momentum integrals appearing in the loop diagrams of the ghost propagator DSE can be solved analytically. This preserves the full analytic momentum dependence and allows evaluating the equation on the real momentum axis. The spectral function can then be directly extracted from the real-time propagator DSE via [Equation \(2\)](#); see [Figure 4a](#) for a comparison to the reconstruction result of the present work. As input gluon spectral function, the reconstruction result of [\[8\]](#) based on the scaling solution obtained via the fRG in [\[6\]](#) is used. Assuming a spectral representation for the gluon propagator, in both scaling and decoupling scenario the infrared behavior of the gluon spectral function follows directly from the propagator [\[8\]](#). This is utilized to modify the given scaling spectral function such that we obtain a decoupling-type gluon propagator matching the value of the given lattice propagator well within the given uncertainties. Due to its mild momentum dependence, the ghost-gluon vertex is assumed to be classical.

The lattice QCD data for the gluon propagator are extended towards the UV using earlier results from functional computations in Yang-Mills theory [\[6\]](#). Differences to the 2+1 flavor QCD result for the gluon propagator reported in [\[11\]](#), being based on [\[7\]](#), are comparably small in the relevant momentum range. A stronger deviation can be observed in the dressing functions, as shown in [Figure 3b](#). Despite these differences, the reconstruction still produces remarkably reliable results, cf. [Figure 1b](#). Nevertheless, we aim to replace the Yang-Mills UV ex-

tension by the 2+1 flavor QCD data from [\[11\]](#) in order to further optimize the accuracy of the result and mitigate any potential issues. For related results and further correlation functions see [\[9, 10, 86, 87\]](#). More specifically, the fRG results in [\[6\]](#) are derived within an advanced approximation where the momentum dependence of all vertices is approximated at the symmetric point, for respective DSE results see [\[88\]](#). For our purposes, this data set provides the optimal trade-off for momentum range versus accuracy. Due to the high numerical precision, the results are particularly well-suited as an input for spectral reconstruction. The Yang-Mills data have already been employed for this purpose in [\[8\]](#) and we use this earlier reconstruction for comparison; see [Figure 4b](#). In summary, the extension of the 2+1 flavor lattice data with the high precision Yang-Mills data up to momenta $p^2 = 10^2 \text{ GeV}^2$ allows a more direct comparison (in terms of scales) with the Yang-Mills reconstruction in [\[8\]](#), while only modifying the large frequency tail of the gluon spectral function for frequencies $\omega \gtrsim 5 \text{ GeV}$, see [Figure 4](#).

Appendix C: Implementation

In this section, we comment on certain points of the implementation in more detail. We first address numerical aspects of the optimization and a discussion of the required computational effort. Subsequently, we provide further information about data usage, kernel design choices and theoretical constraints for the particular reconstructions reported in this work.

1. Hyperparameter Optimization and Computational Cost

To find optimal values for the kernel’s hyperparameters, we perform a fine-grained grid scan of the NLL with additional hyperpriors where necessary. Alternatively, the NLL may also be minimized with a gradient-based ansatz using a standard optimizer such as L-BFGS. However, mapping out the posterior distribution in more detail tends to be highly instructive for the problem at hand. It is also less prone to numerical problems such as unstable directions and violation of positive definiteness of the covariance, as these can be identified early on, and should hence be preferred when feasible. This is also where the bulk of the computational effort goes, as it involves calculating for each individual grid point the comparably expensive inverse and determinant of the covariance matrix, which naively scales like $\mathcal{O}(N^3)$. For very large datasets where their direct evaluation becomes infeasible, one may resort to cheaper linear solvers for the inverse and stochastic approximations of the determinant, but this is unlikely to become necessary in this particular context. Cost may also be mitigated by scanning the parameter space hierarchically, starting at low resolution and zooming into the interesting regions.

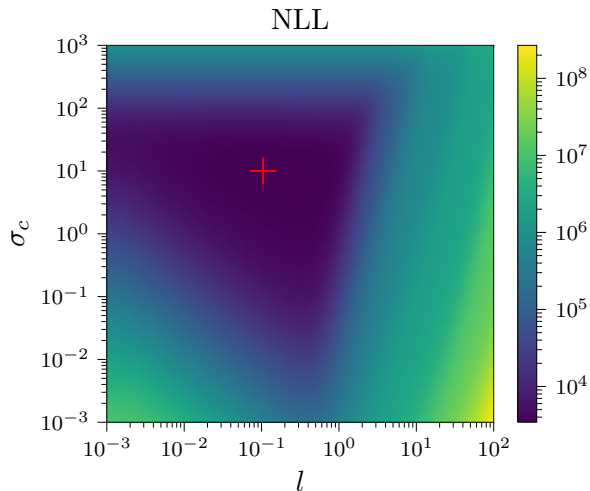


FIG. 5. Heatmap of the NLL as a function of the RBF kernel hyperparameters σ_C, l for the reconstruction of the ghost spectral function, with an additional zero-mean Gaussian hyperprior for σ_C . A unique minimum can be identified, which provides the optimal values used for the results shown in Figures 1a and 2a.

The whole procedure is trivially parallelizable, as each grid point can be treated independently. At the scale of the present work, each instance was handled by a standard CPU node with low performance requirements. Some first tests were also conducted on a single machine, where mapping out the parameter space for each reconstruction with medium resolution took a few hours at most. In comparison to finding the optimal hyperparameters, the subsequent inference step is negligibly cheap. Of course, the total computational effort for the reconstruction is dwarfed by the requirements of the large-scale lattice simulations described in Appendix B 1, which are orders of magnitude more expensive.

2. Reconstruction Details

a. Ghost

In the case of the ghost spectral function, we treat the low-frequency asymptotics extracted from the direct DSE computation in Yang-Mills theory as an additional observation for the GP. This is only possible for the ghost, as a similarly direct determination of the Yang-Mills gluon spectral function is currently not available. The procedure is implemented by including the value of ρ at $\omega = 0$ in the construction of the joint distribution of observations and predictions. In particular, one needs to compute additional expressions for the covariances of the point $\rho(0)$ and the correlator data. This requires some programming headache, but carries no further conceptual difficulty.

As stated in the main text, we use the standard RBF kernel and identify optimal hyperparameters via a high-resolution grid scan. We note an unstable direction in the magnitude parameter σ_C , which is cured by subjecting it to a zero-mean Gaussian hyperprior. As an illustrative example, the heatmap for the NLL including this additional regularization term for σ_C is shown in Figure 5.

b. Gluon

In the case of the gluon spectral function, no real-time result in Yang-Mills theory is available to fix the asymptotics. However, as an additional theoretical constraint we require the solution to respect the aforementioned OZS condition defined in Equation (3). While one might expect this to further complicate the reconstruction, it actually helps in narrowing down the space of plausible solutions. The condition can simply be enforced approximately by treating it as an additional indirect observation and checking it a posteriori. The associated transformation is here just the convolution with ω instead of the KL integral. We confirm that the OZS condition is fulfilled with a relative accuracy of $\sim 1\%$, computed by evaluating the ratio of the left-hand side of Equation (3) and the same expression using the modulus of the integrand, i.e. $\int_0^\infty d\omega |\omega \rho_A(\omega)|$.

As mentioned in the main text, we find it helpful to modify the standard RBF kernel by non-linearly rescaling the frequency as $\omega \rightarrow \tilde{\omega} = \omega^4(1+\omega^4)^{-1}$ before computing the squared distance. This leads to a strongly improved asymptotic stability of the reconstructed spectral function, in particular at large frequencies, compared to just using ω itself. The procedure may be interpreted either as a non-stationary modification of the kernel or as a preprocessing step for the data to the same effect.

- [1] G. Källén. <https://www.e-periodica.ch/digbib/view?pid=hpa-001:1952:25::814>.
- [2] H. Lehmann *Il Nuovo Cimento* **11** no. 4, (Apr., 1954) 342–357.
- [3] A. P. Valentine and M. Sambridge *Geophysical Journal International* **220** no. 3, (11, 2019) 1632–1647.
- [4] S. Zafeiropoulos, P. Boucaud, F. De Soto, J. Rodríguez-Quintero, and J. Segovia *Phys. Rev. Lett.* **122** no. 16, (2019) 162002, [arXiv:1902.08148](https://arxiv.org/abs/1902.08148) [[hep-ph](#)].
- [5] Z.-F. Cui, J.-L. Zhang, D. Binosi, F. de Soto, C. Mezrag, J. Papavassiliou, C. D. Roberts, J. Rodríguez-Quintero, J. Segovia, and S. Zafeiropoulos *Chin. Phys. C* **44** no. 8, (2020) 083102, [arXiv:1912.08232](https://arxiv.org/abs/1912.08232) [[hep-ph](#)].
- [6] A. K. Cyrol, L. Fister, M. Mitter, J. M. Pawłowski, and N. Strodthoff *Phys. Rev. D* **94** no. 5, (2016) 054005, [arXiv:1605.01856](https://arxiv.org/abs/1605.01856) [[hep-ph](#)].
- [7] A. K. Cyrol, M. Mitter, J. M. Pawłowski, and N. Strodthoff *Phys. Rev. D* **97** no. 5, (2018) 054006, [arXiv:1706.06326](https://arxiv.org/abs/1706.06326) [[hep-ph](#)].
- [8] A. K. Cyrol, J. M. Pawłowski, A. Rothkopf, and N. Wink *SciPost Phys.* **5** (2018) 065, [arXiv:1804.00945](https://arxiv.org/abs/1804.00945) [[hep-ph](#)].
- [9] W.-j. Fu, J. M. Pawłowski, and F. Rennecke *Phys. Rev. D* **101** no. 5, (2020) 054032, [arXiv:1909.02991](https://arxiv.org/abs/1909.02991) [[hep-ph](#)].
- [10] F. Gao and J. M. Pawłowski *Phys. Rev. D* **102** no. 3, (2020) 034027, [arXiv:2002.07500](https://arxiv.org/abs/2002.07500) [[hep-ph](#)].
- [11] F. Gao, J. Papavassiliou, and J. M. Pawłowski *Phys. Rev. D* **103** no. 9, (2021) 094013, [arXiv:2102.13053](https://arxiv.org/abs/2102.13053) [[hep-ph](#)].
- [12] J. Horak, J. Papavassiliou, J. M. Pawłowski, and N. Wink [arXiv:2103.16175](https://arxiv.org/abs/2103.16175) [[hep-th](#)].
- [13] J. Braun, Y.-r. Chen, W.-j. Fu, F. Ihssen, J. Horak, C. Huang, J. M. Pawłowski, D. Rennecke, F. Sattler, B. Schallmo, C. Schneider, Y.-y. Tan, S. Töpfer, R. Wen, N. Wink, and S. Yin.
- [14] P. Lowdon *Nucl. Phys. B* **935** (2018) 242–255, [arXiv:1711.07569](https://arxiv.org/abs/1711.07569) [[hep-th](#)].
- [15] P. Lowdon *PoS Confinement2018* (2018) 050, [arXiv:1811.03037](https://arxiv.org/abs/1811.03037) [[hep-th](#)].
- [16] A. Bonanno, T. Denz, J. M. Pawłowski, and M. Reichert [arXiv:2102.02217](https://arxiv.org/abs/2102.02217) [[hep-th](#)].
- [17] R. Oehme and W. Zimmermann *Phys. Rev.* **D21** (1980) 1661.
- [18] R. Oehme *Phys. Lett.* **B252** (1990) 641–646.
- [19] G. Cuniberti, E. De Micheli, and G. A. Viano *Commun. Math. Phys.* **216** (2001) 59–83, [arXiv:cond-mat/0109175](https://arxiv.org/abs/cond-mat/0109175) [[cond-mat.str-el](#)].
- [20] Y. Burnier, M. Laine, and L. Mether *Eur. Phys. J. C* **71** (2011) 1619, [arXiv:1101.5534](https://arxiv.org/abs/1101.5534) [[hep-lat](#)].
- [21] M. Jarrell and J. E. Gubernatis *Phys. Rept.* **269** (1996) 133–195.
- [22] M. Asakawa, T. Hatsuda, and Y. Nakahara *Prog. Part. Nucl. Phys.* **46** (2001) 459–508, [arXiv:hep-lat/0011040](https://arxiv.org/abs/hep-lat/0011040) [[hep-lat](#)].
- [23] M. Haas, L. Fister, and J. M. Pawłowski *Phys. Rev. D* **90** (2014) 091501, [arXiv:1308.4960](https://arxiv.org/abs/1308.4960) [[hep-ph](#)].
- [24] Y. Burnier and A. Rothkopf *Phys. Rev. Lett.* **111** (2013) 182003, [arXiv:1307.6106](https://arxiv.org/abs/1307.6106) [[hep-lat](#)].
- [25] A. Rothkopf *Phys. Rev.* **D95** no. 5, (2017) 056016, [arXiv:1611.00482](https://arxiv.org/abs/1611.00482) [[hep-ph](#)].
- [26] J. Fei, C.-N. Yeh, and E. Gull *Physical Review Letters* **126** no. 5, (Feb, 2021) 056402, [arXiv:2010.04572](https://arxiv.org/abs/2010.04572) [[cond-mat.str-el](#)].
- [27] J. Fei, C.-N. Yeh, D. Zgid, and E. Gull [arXiv:2107.00788](https://arxiv.org/abs/2107.00788) [[cond-mat.str-el](#)].
- [28] D. Binosi and R.-A. Tripolt *Phys. Lett. B* **801** (2020) 135171, [arXiv:1904.08172](https://arxiv.org/abs/1904.08172) [[hep-ph](#)].
- [29] M. Ulybyshev, C. Winterowd, and S. Zafeiropoulos *Phys. Rev. B* **96** no. 20, (2017) 205115, [arXiv:1707.04212](https://arxiv.org/abs/1707.04212) [[cond-mat.str-el](#)].
- [30] D. Dudal, O. Oliveira, M. Roelfs, and P. Silva *Nucl. Phys. B* **952** (2020) 114912, [arXiv:1901.05348](https://arxiv.org/abs/1901.05348) [[hep-lat](#)].
- [31] D. Dudal, O. Oliveira, and M. Roelfs [arXiv:2103.11846](https://arxiv.org/abs/2103.11846) [[hep-lat](#)].
- [32] R. Fournier, L. Wang, O. V. Yazyev, and Q. Wu *Physical Review Letters* **124** no. 5, (Feb, 2020) 056401, [arXiv:1810.00913](https://arxiv.org/abs/1810.00913) [[physics.comp-ph](#)].
- [33] H. Yoon, J.-H. Sim, and M. J. Han *Physical Review B* **98** no. 24, (Dec, 2018) 245101, [arXiv:1806.03841](https://arxiv.org/abs/1806.03841) [[cond-mat.str-el](#)].
- [34] L. Kades, J. M. Pawłowski, A. Rothkopf, M. Scherzer, J. M. Urban, S. J. Wetzel, N. Wink, and F. P. G. Ziegler *Phys. Rev. D* **102** no. 9, (2020) 096001, [arXiv:1905.04305](https://arxiv.org/abs/1905.04305) [[physics.comp-ph](#)].
- [35] M. Zhou, F. Gao, J. Chao, Y.-X. Liu, and H. Song [arXiv:2106.08168](https://arxiv.org/abs/2106.08168) [[hep-ph](#)].
- [36] L.-F. Arsenault, R. Neuberg, L. A. Hannah, and A. J. Millis [arXiv:1612.04895](https://arxiv.org/abs/1612.04895) [[cond-mat.str-el](#)].
- [37] S. Offer, G. Aarts, C. Allton, J. Glesaaen, B. Jäger, S. Kim, M. P. Lombardo, S. M. Ryan, and J.-I. Skullerud *PoS LATTICE2019* (2019) 076, [arXiv:1912.12900](https://arxiv.org/abs/1912.12900) [[hep-lat](#)].
- [38] D. G. Krige *Journal of the Southern African Institute of Mining and Metallurgy* **52** no. 6, (1951) 119–139.
- [39] M. Kanagawa, P. Hennig, D. Sejdinovic, and B. K. Sriperumbudur [arXiv:1807.02582](https://arxiv.org/abs/1807.02582) [[stat.ML](#)].
- [40] H. Liu, Y.-S. Ong, X. Shen, and J. Cai [arXiv:1807.01065](https://arxiv.org/abs/1807.01065) [[stat.ML](#)].
- [41] C. E. Rasmussen and C. K. I. Williams, *Gaussian Processes for Machine Learning (Adaptive Computation and Machine Learning)*. The MIT Press, 2005.
- [42] F. D. R. Bonnet, P. O. Bowman, D. B. Leinweber, and A. G. Williams *Phys. Rev. D* **62** (2000) 051501, [arXiv:hep-lat/0002020](https://arxiv.org/abs/hep-lat/0002020).
- [43] A. Sternbeck, E. M. Ilgenfritz, M. Müller-Preussker, and A. Schiller *Phys. Rev. D* **72** (2005) 014507, [arXiv:hep-lat/0506007](https://arxiv.org/abs/hep-lat/0506007).
- [44] P. Boucaud, J. P. Leroy, A. Le Yaouanc, A. Y. Lokhov, J. Micheli, O. Pene, J. Rodríguez-Quintero, and C. Roiesnel *Phys. Rev. D* **72** (2005) 114503, [arXiv:hep-lat/0506031](https://arxiv.org/abs/hep-lat/0506031).
- [45] P. J. Silva and O. Oliveira *Phys. Rev. D* **74** (2006) 034513, [arXiv:hep-lat/0511043](https://arxiv.org/abs/hep-lat/0511043).
- [46] A. Cucchieri, A. Maas, and T. Mendes *Phys. Rev. D* **74** (2006) 014503, [arXiv:hep-lat/0605011](https://arxiv.org/abs/hep-lat/0605011).
- [47] A. Cucchieri, A. Maas, and T. Mendes *Phys. Rev. D* **77** (2008) 094510, [arXiv:0803.1798](https://arxiv.org/abs/0803.1798) [[hep-lat](#)].
- [48] O. Oliveira and P. J. Silva *Phys. Rev. D* **79** (2009)

- 031501, [arXiv:0809.0258 \[hep-lat\]](#).
- [49] I. L. Bogolubsky, E. M. Ilgenfritz, M. Muller-Preussker, and A. Sternbeck *Phys. Lett. B* **676** (2009) 69–73, [arXiv:0901.0736 \[hep-lat\]](#).
- [50] T. Iritani, H. Suganuma, and H. Iida *Phys. Rev. D* **80** (2009) 114505, [arXiv:0908.1311 \[hep-lat\]](#).
- [51] A. Ayala, A. Bashir, D. Binosi, M. Cristoforetti, and J. Rodríguez-Quintero *Phys. Rev. D* **86** (2012) 074512, [arXiv:1208.0795 \[hep-ph\]](#).
- [52] A. Athenodorou, P. Boucaud, F. De Soto, J. Rodríguez-Quintero, and S. Zafeiropoulos *EPJ Web Conf.* **175** (2018) 12012, [arXiv:1802.00698 \[hep-lat\]](#).
- [53] A. G. Duarte, O. Oliveira, and P. J. Silva *Phys. Rev. D* **94** no. 7, (2016) 074502, [arXiv:1607.03831 \[hep-lat\]](#).
- [54] A. C. Aguilar, F. De Soto, M. N. Ferreira, J. Papavassiliou, J. Rodríguez-Quintero, and S. Zafeiropoulos *Eur. Phys. J. C* **80** no. 2, (2020) 154, [arXiv:1912.12086 \[hep-ph\]](#).
- [55] A. C. Aguilar, F. De Soto, M. N. Ferreira, J. Papavassiliou, and J. Rodríguez-Quintero *Phys. Lett. B* **818** (2021) 136352, [arXiv:2102.04959 \[hep-ph\]](#).
- [56] A. C. Aguilar, C. O. Ambrósio, F. De Soto, M. N. Ferreira, B. M. Oliveira, J. Papavassiliou, and J. Rodríguez-Quintero [arXiv:2107.00768 \[hep-ph\]](#).
- [57] I. C. Cloet and C. D. Roberts *Prog. Part. Nucl. Phys.* **77** (2014) 1–69, [arXiv:1310.2651 \[nucl-th\]](#).
- [58] G. Eichmann, H. Sanchis-Alepuz, R. Williams, R. Alkofer, and C. S. Fischer *Prog. Part. Nucl. Phys.* **91** (2016) 1–100, [arXiv:1606.09602 \[hep-ph\]](#).
- [59] H. Sanchis-Alepuz and R. Williams *Comput. Phys. Commun.* **232** (2018) 1–21, [arXiv:1710.04903 \[hep-ph\]](#).
- [60] N. Christiansen, M. Haas, J. M. Pawłowski, and N. Strodthoff *Phys. Rev. Lett.* **115** no. 11, (2015) 112002, [arXiv:1411.7986 \[hep-ph\]](#).
- [61] M. Bluhm *et al. Nucl. Phys. A* **1003** (2020) 122016, [arXiv:2001.08831 \[nucl-th\]](#).
- [62] C. S. Ong, A. J. Smola, and R. C. Williamson *Journal of Machine Learning Research* **6** no. 36, (2005) 1043–1071.
- [63] A. G. Wilson, Z. Hu, R. Salakhutdinov, and E. P. Xing [arXiv:1511.02222 \[cs.LG\]](#).
- [64] J. Horak, J. M. Pawłowski, and N. Wink *Phys. Rev. D* **102** (2020) 125016, [arXiv:2006.09778 \[hep-th\]](#).
- [65] M. Krasser. <https://krasserm.github.io/2018/03/19/gaussian-processes/>.
- [66] W. Menke and R. Creel *Surveys in Geophysics* **42** no. 3, (Apr., 2021) 473–503.
- [67] D. Duvenaud. <https://www.cs.toronto.edu/~duvenaud/cookbook/>.
- [68] **RBC, UKQCD** Collaboration, C. Allton *et al. Phys. Rev. D* **76** (2007) 014504, [arXiv:hep-lat/0701013 \[hep-lat\]](#).
- [69] **RBC-UKQCD** Collaboration, C. Allton *et al. Phys. Rev. D* **78** (2008) 114509, [arXiv:0804.0473 \[hep-lat\]](#).
- [70] **RBC, UKQCD** Collaboration, R. Arthur *et al. Phys. Rev. D* **87** (2013) 094514, [arXiv:1208.4412 \[hep-lat\]](#).
- [71] **RBC, UKQCD** Collaboration, T. Blum *et al. Phys. Rev. D* **93** no. 7, (2016) 074505, [arXiv:1411.7017 \[hep-lat\]](#).
- [72] P. A. Boyle, L. Del Debbio, A. Jüttner, A. Khamseh, F. Sanfilippo, and J. T. Tsang *JHEP* **12** (2017) 008, [arXiv:1701.02644 \[hep-lat\]](#).
- [73] Y. Iwasaki *Nucl. Phys.* **B258** (1985) 141–156.
- [74] D. B. Kaplan *Phys. Lett.* **B288** (1992) 342–347, [arXiv:hep-lat/9206013 \[hep-lat\]](#).
- [75] Y. Shamir *Nucl. Phys.* **B406** (1993) 90–106, [arXiv:hep-lat/9303005 \[hep-lat\]](#).
- [76] R. C. Brower, H. Neff, and K. Orginos *Nucl. Phys. Proc. Suppl.* **140** (2005) 686–688, [arXiv:hep-lat/0409118 \[hep-lat\]](#).
- [77] A. Sternbeck, K. Maltman, L. von Smekal, A. G. Williams, E. M. Ilgenfritz, and M. Muller-Preussker *PoS LATTICE2007* (2007) 256, [arXiv:0710.2965 \[hep-lat\]](#).
- [78] P. Boucaud, F. De Soto, J. Leroy, A. Le Yaouanc, J. Micheli, O. Pène, and J. Rodríguez-Quintero *Phys. Rev. D* **79** (2009) 014508, [arXiv:0811.2059 \[hep-ph\]](#).
- [79] A. Sternbeck *et al. PoS LAT2009* (2009) 210, [arXiv:1003.1585](#).
- [80] D. Binosi, C. Mezrag, J. Papavassiliou, C. D. Roberts, and J. Rodríguez-Quintero *Phys. Rev. D* **96** no. 5, (2017) 054026, [arXiv:1612.04835 \[nucl-th\]](#).
- [81] P. Boucaud, F. De Soto, K. Raya, J. Rodríguez-Quintero, and S. Zafeiropoulos *Phys. Rev. D* **98** no. 11, (2018) 114515, [arXiv:1809.05776 \[hep-ph\]](#).
- [82] D. Binosi and J. Papavassiliou *Phys. Rept.* **479** (2009) 1–152, [arXiv:0909.2536 \[hep-ph\]](#).
- [83] M. Q. Huber *Phys. Rept.* **879** (2020) 1–92, [arXiv:1808.05227 \[hep-ph\]](#).
- [84] C. S. Fischer *Prog. Part. Nucl. Phys.* **105** (2019) 1–60, [arXiv:1810.12938 \[hep-ph\]](#).
- [85] N. Dupuis, L. Canet, A. Eichhorn, W. Metzner, J. M. Pawłowski, M. Tissier, and N. Wschebor *Phys. Rept.* **910** (2021) 1–114, [arXiv:2006.04853 \[cond-mat.stat-mech\]](#).
- [86] A. C. Aguilar, D. Binosi, and J. Papavassiliou *Phys. Rev. D* **86** (2012) 014032, [arXiv:1204.3868 \[hep-ph\]](#).
- [87] R. Williams, C. S. Fischer, and W. Heupel *Phys. Rev. D* **93** no. 3, (2016) 034026, [arXiv:1512.00455 \[hep-ph\]](#).
- [88] M. Q. Huber *Phys. Rev. D* **101** (2020) 114009, [arXiv:2003.13703 \[hep-ph\]](#).